Chenbin Ma *et al*.: PPG-based Continuous BP Waveform Estimation Using Polarized Attention-guided Conditional Adversarial Learning Model

1

PPG-based Continuous BP Waveform Estimation Using Polarized Attention-guided Conditional Adversarial Learning Model

Chenbin Ma, Yangfan Xu, Peng Zhang, Fan Song, Yangyang Sun, Youdan Feng, Yufang He, Guanglei Zhang, *Member, IEEE*

Abstract—The blood pressure (BP) waveform is a vital source of physiological and pathological information concerning the cardiovascular system. This study proposes a novel attention-guided conditional generative adversarial network (cGAN), named PPG2BP-cGAN, to estimate BP waveforms based on photoplethysmography (PPG) signals. The proposed model comprises a generator and a discriminator. Specifically, the UNet3+-based generator integrates a full-scale skip connection structure with a modified polarized self-attention module based on a spatial-temporal attention mechanism. Additionally, its discriminator comprises PatchGAN, which augments the discriminative power of the generated BP waveform by increasing the perceptual field through fully convolutional layers. We demonstrate the superior BP waveform prediction performance of our proposed method compared to state-of-the-art (SOTA) techniques on two independent datasets. Our approach first pre-trained on a dataset containing 683 subjects and then tested on a public dataset. Experimental results from the Multi-parameter Intelligent Monitoring in Intensive Care dataset show that the proposed method achieves a root mean square error of 3.54, mean absolute error of 2.86, and Pearson coefficient of 0.99 for BP waveform estimation. Furthermore, the estimation errors (mean error ± standard deviation error) for systolic BP and diastolic BP are 0.72 ± 4.34 mmHg and 0.41 ± 2.48 mmHg, respectively, meeting the American Association for the Advancement of Medical Instrumentation standard. Our approach exhibits significant superiority over SOTA techniques on independent datasets, thus highlighting its potential for future applications in continuous cuffless BP waveform measurement.

Index Terms—Blood pressure waveform, photoplethysmography, conditional adversarial network, deep learning, attention mechanism

C. Ma and Y. Xu devoted equal contribution. Corresponding Author: Guanglei Zhang (e-mail: guangleizhang@buaa.edu.cn)

C. Ma is with the Beijing Advanced Innovation Center for Biomedical Engineering, School of Biological Science and Medical Engineering, Beihang University, Beijing 100191, China, and also with the Shen Yuan Honors College, Beihang University, Beijing, 100191, China (e-mail: machenbin@buaa.edu.cn).

Y. Xu, P. Zhang, F. Song, Y. Sun, Y. Feng, Y. He, G. Zhang are with the Beijing Advanced Innovation Center for Biomedical Engineering, School of Biological Science and Medical Engineering, Beihang University, Beijing 100191, China (e-mail: xuyf22@mails.tsinghua.edu.cn, {pengzhang, fansong, syyzbh, emilyfeng, heihey, guangleizhang}@buaa.edu.cn).

I. INTRODUCTION

In the past 20 years, cardiovascular mortality in low- and middle-income countries has increased by nearly 50% [1], with an estimated incidence of about 30% higher than in high-income countries [2], according to data from the World Health Organization database. This highlights the need for improved prognostic outcomes, care burden reduction, and reduced mortality. In this context, low-cost continuous ambulatory blood pressure (BP) monitoring technology could serve as a promising solution [3]. Clinical studies reveal that certain abnormal information is implicated in the arterial BP waveform early in the development of cardiovascular diseases, such as irregular waveforms suggesting arrhythmias or small fluctuations indicating the presence of arterial plaque [3]. Thus, noninvasive monitoring methods that can accurately capture continuous BP waveforms are crucial.

While invasive arterial cannulation is the gold standard for obtaining continuous BP waveforms, it poses pain and infection risks. Therefore, noninvasive BP monitoring methods are more appropriate for health management outside the intensive care unit (ICU). In addition, if the BP waveform of each cardiac cycle and the trend of BP changes over a period of time could be continuously monitored noninvasively, richer physiological information could be obtained for effective prevention and diagnosis, and treatment of cardiovascular diseases. Nonetheless, traditional noninvasive methods that require cuffs, such as auscultation and oscillometric techniques, obstruct blood vessels during testing do not support long-term continuous monitoring. A novel cuffless BP measurement method that acquires pulse waveforms through advanced sensing such as photoplethysmography (PPG) [4-8], radar [9], or ultrasound [10] offers a promising direction. Incorporating pulse transit time (PTT) and combining ballistocardiogram (BCG) [11] or electrocardiogram (ECG) [12-17] signals, this method allows for the estimation of continuous BP waveforms with high accuracy.

Recently, deep learning-based methods have been proposed to address the challenge of cuffless BP waveform estimation. Compared to traditional machine learning methods that require manual extraction of PPG morphological features, deep learning methods automatically learn the best features necessary for mapping PPG signals onto BP waveforms. There

Chenbin Ma *et al.*: PPG-based Continuous BP Waveform Estimation Using Polarized Attention-guided Conditional Adversarial Learning Model

2

are some methods of estimating BP waveform, autoregressive models [8, 14], deep convolutional autoencoder (DCAE) [18], UNet [19], V-Net [20], and KD-Informer [21] models. However, most existing methods do not fully meet the standards established by the advancement of medical instrumentation (AAMI) due to their inadequate number of datasets or model performance [14, 18, 22-25]. Moreover, the traditional sample-wise data division paradigm employed in these methods may lead to an overly optimistic estimation of errors, as the samples used to evaluate the model may come from the same individuals used in the training set.

Given that the BP waveform estimation problem can be viewed as a distribution transformation problem from PPG signal to BP waveform, we propose using a conditional generative adversarial network (cGAN), called PPG2BP-cGAN, as an interpretable backbone for supervised BP waveform estimation. Our method introduces full-scale skip connections into the cGAN, which significantly improves the computational efficiency of the full-scale feature maps. We also incorporate the perceptual loss into the jointly optimized objective function to accurately capture the fine details of the BP waveform reconstruction. Additionally, we present the modified polarized self-attention (MPSA), a spatial-temporal attention mechanism, within the cGAN model to focus on predicting the peaks and valleys of BP waveforms.

Our study synergistically integrates the attention mechanism and full-scale feature fusion within the cGAN model and demonstrates that the proposed method effectively and robustly estimates BP waveforms in two independent datasets. Hence, our work contributes to the ongoing efforts to develop practical and accurate cuffless methods for continuous BP monitoring with potential implications for the effective prevention, diagnosis, and treatment of cardiovascular diseases.

II. Related Works

Over the past few decades, various PPG-based methods have been proposed for cuffless BP estimation. Pulse wave velocity theory methods are one of them [26], which can continuously monitor BP values and avoid intermittent measurements with cuff devices. However, these methods necessitate simultaneous measurement of PPG signals at multiple points [26] or ECG signals [12-14, 16, 17] to calculate PTT, making it inconvenient for users. To reduce costs, data-driven models have been proposed to directly map input PPG signals to BP values [4-8] with higher estimation accuracy. Nonetheless, these models require calibration algorithms, frequently demand individualized modeling, and do not offer continuous BP waveform estimates.

In recent years, deep learning-based methods have been proposed to address the problem of estimating the BP waveform [8, 14, 18-21]. For example, the autoregressive model can obtain the time delay information of each data point in the PPG signal for effectively identifying different cardiovascular states. The sequenced-to-sequenced (Seq2Seq) method based on autoregressive models obtains the probability of maximizing BP waveforms by learning the conditional distribution of PPG signals and searching for phylogenetic trees

that occur with higher probability using maximum likelihood estimation [8]. However, the Seq2Seq model lacks long-term dependence, and its standard deviation error (SED) regarding systolic BP (SBP) is as high as 15.67 mmHg [8], unsatisfying the AAMI standard (SDE should not exceed 8 mmHg).

On the other hand, autoencoders have better predictive performance [18-20]. They use the encoder to extract features from the PPG signal by reducing the length of the input signal while increasing its depth. Thus, the encoder performs a latent space representation of the PPG signal. Then the decoder decodes the latent vector in the bottleneck into the corresponding BP waveform. However, the function mapping is lost when the information is passed from the encoder to the decoder. Therefore, some approaches concatenate the decoder layer with the corresponding encoder layer to compensate for the features lost when reconstructing the BP waveform. For example, the V-Net model based on skip connection has been shown to reduce the SDE of SBP to 6.53 mmHg but increase the ME to 4.30 mmHg [20]. Recently, Mehrabadi et al. [27] employed an unsupervised image-to-image translation model, i.e., CycleGAN [28], to fit paired PPG-BP data. Specifically, CycleGAN is trained in an unsupervised process using generative networks, and its cyclic consistency avoids the mode-collapse problem. However, the performance of this model on paired data is relatively lower than that of other image transcription models [28]. Ma et al. [21] proposed a Transformer-based method with knowledge distillation for BP waveform estimation. Benefiting from elaborate morphological features, the KD-Informer still performs superior BP estimation in a subject-wise paradigm. Their results display the BP waveform estimates for a randomly selected sample in terms of root mean square error (RMSE), mean absolute error (MAE), and Pearson coefficients (R^2) of 7.27, 2.23, and 0.99 mmHg, respectively. However, they do not demonstrate the average results of BP waveform estimation and do not compare them with the British hypertension society (BHS) standard.

III. Methodology

A. Problem Formulation

BP waveform estimation based on adversarial learning can usually be viewed as a sequence-to-sequence transformation. Here, the original PPG signal space $\mathcal{X} \in \mathbb{R}^{s_x \times d_x \times M}$ and corresponding target BP signal space $\mathcal{Y} \in \mathbb{R}^{s_y \times M}$ give paired samples $\{(x_i, y_i) \mid x_i \in \mathcal{X}, y_i \in \mathcal{Y}\}_{i=1}^{M}$. The PPG signal with samples s_x and dimension d_x and BP signal with s_y samples have one-to-one correspondence for the M-segment data. Our generator learns a mapping from PPG signal x and random noise vector z to y:

$$G : \{x, z\} \to y \qquad (1)$$

and the discriminator is trained to determine whether the BP waveform estimated by the generator is a fake signal.

Chenbin Ma *et al*.: PPG-based Continuous BP Waveform Estimation Using Polarized Attention-guided Conditional Adversarial Learning Model

3

B. Derivation of PPG2BP-cGAN

GANs consist of a generator with parameters $G_\theta(\bullet)$ and a discriminator with parameters $D_\phi(\bullet)$. The generator $G_\theta(\bullet)$ receives a sample z from prior noise distribution p_{noise} as input, and its task is to map it to the target space $\hat{x} = G_\theta(z)$ to produce a model distribution $p(\hat{x})$. Further, the discriminator $D_\phi(\bullet)$ is a binary classifier that aims to classify true samples $x \sim p(\mathcal{X})$ as real when $D_\phi(x) = 1$, and generated samples $\hat{x} \sim p(\hat{\mathcal{X}})$ as fake when $D_\phi(\hat{x}) = 0$. These two networks perform adversarial learning through the game-theoretic principle of the min-max optimization task:

$$G^* = \arg\min_G \max_D \mathcal{L}_{GAN} \qquad (2)$$

where adversarial loss $\mathcal{L}_{GAN}$ is given by:

$$\mathcal{L}_{GAN} = \mathbb{E}_{x \sim p(\mathcal{X})}[\log D_\phi(x)] \\ + \mathbb{E}_{z \sim p_{noise}}[1 - \log D_\phi(G_\theta(z))] \qquad (3)$$

In estimating BP waveforms based on PPG signals, the purpose of the generator is to map the source domain signal $x \sim p_{source}(\mathcal{X})$ to its corresponding ground truth target signal $y \sim p_{target}(\mathcal{Y})$ by the mapping function $G_\theta(x,z) \to \hat{y}$. We employ the one-to-one correspondence between PPG signals and BP waveforms as conditional information for our cGAN framework, which enables our model to learn both the mapping and pairing relationships between distribution $\mathcal{X}$ and $\mathcal{Y}$. This, in turn, allows us to control the input PPG signal x_i to generate a specific BP waveform y_i. In this case, the adversarial loss $\mathcal{L}_{cGAN}$ is given by:

$$\mathcal{L}_{cGAN} = \mathbb{E}_{x \sim p(\mathcal{X})}[\log D_\phi(x \mid y)] \\ + \mathbb{E}_{z \sim p_{noise}}[\log(1 - D_\phi(G_\theta(z \mid y)))] \qquad (4)$$

Traditional image-to-image translation methods usually add pixel reconstruction losses, such as L1 loss, to the adversarial loss so that the generated image may have a similar global structure to the ground truth image [29]. Inspired by these works, we also calculate the MAE between the generated and real BP waveforms as follows:

$$\mathcal{L}_{L_1} = \mathbb{E}_{x,y,z}\left[\|y - G_\theta(x,z)\|_1\right] \qquad (5)$$

The pixel-like reconstruction loss maintains the global refinement structure at the risk of distortion and loss of detail, often leading to distortion and phase shift in the generated BP waveform, i.e., the high-frequency component of the signal [30, 31] is disrupted. Accurate estimation of BP patterns is critical, as fluctuations and lags in the BP waveform can significantly impact clinical diagnostic decisions. Therefore, a perceptual loss is utilized to capture the difference between the estimated and the reference high-frequency components of the BP waveform [30, 31]. This loss is extracted through a discriminator network and a trainable feature extractor for the intermediate feature representation. The MAE between the

i-th feature map of the reference BP waveform y and the generated BP waveform $\hat{y}$ is computed as:

$$\mathcal{P}_{L_1}^i(G_\theta(x,z),y) = \frac{1}{L^i \cdot C^i}\left\|D_\phi^i(G_\theta(x,z),x) - D_\phi^i(x,y)\right\|_1 \quad (6)$$

where $D_\phi^i(\bullet)$ refers to the feature map extracted from the i-th hidden layer of the discriminator $D_\phi(\bullet)$, L^i and C^i denote the length and the number of channels of the feature space, respectively. For a discriminator with N hidden layers, the perceptual loss can be calculated as follows:

$$\mathcal{L}_{perceptual} = \sum_{i=0}^{N} \lambda_p^i \mathcal{P}_{L_1}^i(G_\theta(x,z),y) \qquad (7)$$

where $\lambda_p^i > 0$ corresponds to the prior optimization parameters of the i-th layer.

In addition, we calculate the mean square error (MSE) between the reference BP waveform and the estimated waveform at the systolic and diastolic amplitudes to facilitate the model to predict SBP and diastolic BP (DBP) values accurately:

$$\mathcal{L}_{sl2} = \mathbb{E}_{x,y,z}\left[\|peak(y) - peak(G_\theta(x,z))\|_2\right] \qquad (8)$$

$$\mathcal{L}_{dl2} = \mathbb{E}_{x,y,z}\left[\|valley(y) - valley(G_\theta(x,z))\|_2\right] \qquad (9)$$

By putting them together, our final optimization problem for BP waveform estimation can be given:

$$G^* = \arg\min_G \max_D \mathcal{L}_{PPG2BP-cGAN}(\theta,\phi) \qquad (10)$$

where

$$\mathcal{L}_{PPG2BP-cGAN}(\theta,\phi) \coloneqq \mathcal{L}_{cGAN}(\theta,\phi) + \lambda\mathcal{L}_{L_1}(\theta) \\ + \gamma\mathcal{L}_{perceptual}(\theta) + \delta\mathcal{L}_{sl2} + \xi\mathcal{L}_{dl2} \qquad (11)$$

where $\lambda, \gamma, \delta, \xi \geq 0$ are the hyperparameters for these corresponding losses. The resulting network architecture is illustrated in Fig. 1.

C. Attention Mechanism

In Fig. 1, we illustrate the presence of similar ascending and descending patterns between PPG and BP waveforms. The peaks and valleys of the BP waveform correspond directly to physiological values such as SBP and DBP and reflect factors such as cardiac pumping function and blood physical state [32]. Therefore, we introduce the MPSA mechanism (shown in Fig. 2), which uses polarized filtering to effectively integrate spatial and temporal dimensions, thereby enabling dual attention [33]. Precise estimation of fine-grained BP waveforms demands a model capable of capturing long-range dependencies among high-resolution input/output features while maintaining computational efficiency, for accurate estimation of both nonlinear signal values and semantic trend features. In recent years, attentional modules within deep neural networks have been inspired by attention mechanisms in the human visual system. By emulating the capacity of humans to selectively

Chenbin Ma *et al*.: PPG-based Continuous BP Waveform Estimation Using Polarized Attention-guided Conditional Adversarial Learning Model

4

focus on salient features through multiple glimpses, our proposed MPSA mechanism improves the performance of

fine-grained BP waveform capture, enabling effective prediction of the peaks and valleys of BP waveforms.
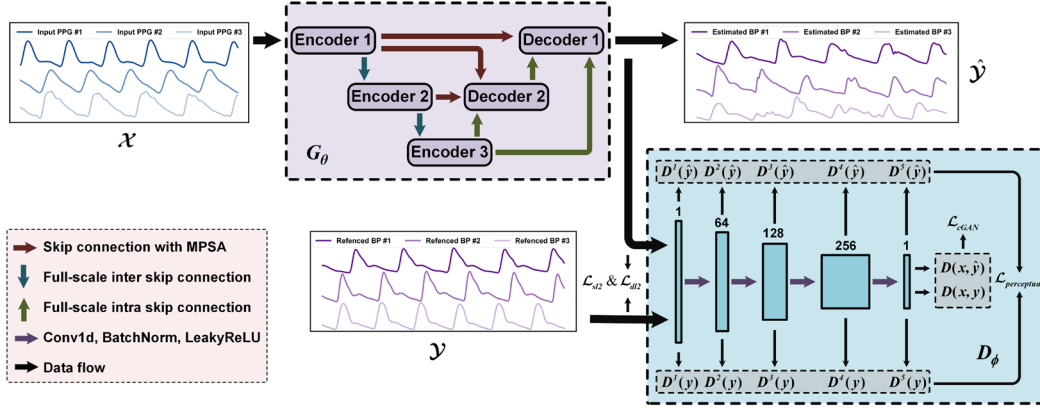

Fig. 1. The overall architecture of the PPG2BP-cGAN model, including a novel UNet3+-based generator and a PatchGAN-based discriminator architecture. The task of the generator $G_\theta(\bullet)$ is to transform the input PPG signals from the source domain $x \sim p_{source}(\mathcal{X})$ to the target domain $y \sim p_{target}(\mathcal{Y})$ (i.e., the estimated BP waveform) through a stepwise refinement of the encoder-decoder module. The adversarial discriminator $D_\phi(\bullet)$ is trained to distinguish the real BP waveform $\mathcal{Y}$ from the transformed BP waveform $\hat{y}$ and to provide corrected cGAN loss $\mathcal{L}_{cGAN}$ perceptual loss $\mathcal{L}_{perceptual}$. Further, we defined the L2 loss $\mathcal{L}_{sl2}$ and $\mathcal{L}_{dl2}$ between the reference BP waveform and the estimated waveform at the systolic and diastolic point locations to facilitate the model to predict SBP and DBP values accurately.

Specifically, we use $H = \{h_i\}_{i=1}^C \in \mathbb{R}^{C \times L}$ to denote the feature map, and the attended feature map $\hat{H} \in \mathbb{R}^{C \times L}$ is computed by matrix multiplication:

$$\hat{H} = THS \quad (12)$$

where $S \in \mathbb{R}^{C \times C}$ corresponds to a spatial attention map and $T \in \mathbb{R}^{L \times L}$ is a temporal attention map. In the following, we describe MPSA in more detail.

1) Spatial Attention Module. The spatial attention module focuses on the feature channels that contribute more to the representation of the BP waveform. As shown in Fig. 3, we transform the input feature map H into query Q and key K using convolution layers W_q and W_k with the kernels of size 1, where Q channels are fully compressed, and the information is augmented by Softmax-based high dynamic range. Then Q and K are matrix multiplied and followed by a convolution W_z, layer normalization (LN), to raise the dimensionality of $C/2$ on the channels to C:

$$A^{sp}(H) = SG\left[W_{z|\kappa_1}\left(\left(\psi_1(W_k(H)) \times SM(\psi_2(W_q(H))) \right) \right) \right] (13)$$

where $A^{sp}(H) \in \mathbb{R}^{C \times 1}$, ψ_1 and ψ_2 are two tensor-reshape operators, and κ_1 is an intermediate parameter for these channel convolutions. SG and SM represent the Sigmoid and Softmax operators, respectively. As shown in Fig. 3, we can get the output of spatial attention as $Z^{sp} = A^{sp}(H) \odot^{ch} H \in \mathbb{R}^{C \times L}$, where $\odot^{ch}$ is a channel-wise multiplication operator.

2) Temporal Attention Module. The temporal attention module assigns weights to the time segments of the feature map to focus on the more informative segments of the PPG signal. Similar to the spatial attention module, the input features are first converted to Q and K using a convolution with one kernel

size, as shown in Fig. 3. In this case, the spatial dimension of the Q value is compressed using global pooling. In contrast, the spatial dimension of the K value is kept at the original scale. Next, the information of Q is augmented using Softmax. Then Q and K are matrix multiplied and $A^{tm}(H) \in \mathbb{R}^{1 \times L}$ can be obtained as follows:

$$A^{tm}(H) = SG\left[\psi_3\left(SM\left(\psi_1\left(GP\left(W_q(H) \right) \right) \right) \times \psi_2\left(W_k(H) \right) \right) \right] (14)$$

where ψ_3 is a tensor reshape operator, and GP represents the global pooling operator. The output of temporal attention is $Z^{tm} = A^{tm}(H) \odot^{tm} H \in \mathbb{R}^{C \times L}$, where $\odot^{tm}$ is a temporal-wise multiplication operator.

3) Composition. Inspired by the polarized self-attention experiment results, the outputs of the above two modules are composed under a parallel layout to form the MPSA:

$$\begin{aligned} MPSA(H) &= Z^{sp} + Z^{tm} \\ &= A^{sp}(H) \odot^{ch} H + A^{tm}(H) \odot^{tm} H \end{aligned} \quad (15)$$

where + is the element-wise addition operator. As shown in Fig. 1 and Fig. 4, we added MPSA to the skip and the concatenation layers to emphasize the representative local features along spatial and temporal axes in PPG signals.
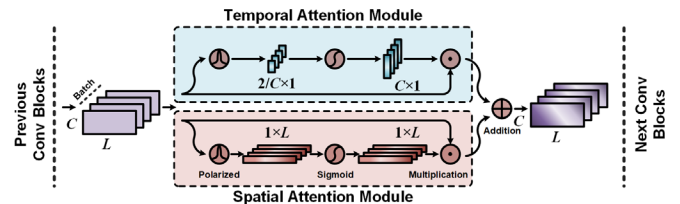

Fig. 2. Schematic diagram of the architecture of the proposed plug-and-play modified polarized self-attention (MPSA) module embedded in the model. The MPSA module keeps high internal

Chenbin Ma *et al*.: PPG-based Continuous BP Waveform Estimation Using Polarized Attention-guided Conditional Adversarial Learning Model

5

resolution along the spatial ($C/2$) and temporal dimension (L) while collapsing the input feature maps ($[C \times L]$) along their counterparts' dimensions. Further, they fit output distributions of sample-wise regression with a sigmoid composition operation.
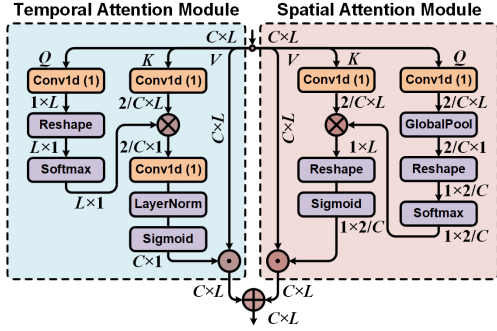

Fig. 3. The schematic diagram modified polarized self-attention (MPSA) mechanism, where Conv1d (1) denotes the one-dimensional convolution operator with a kernel of size 1, GlobalPool denotes the global pooling operator, and LayerNorm denotes layer normalization.

D. Network Architecture

1) UNet3+-based Generator. The success of pix2pix shows that skip connections via UNet [34] can avoid the limitation of bottleneck layers in encoding-decoding networks for low-level shared information [29]. Fig. 4(a) depicts that we employ UNet3+ [35] as the backbone of generator to capture fine-grained details and coarse-grained semantics more effectively. Moreover, we adopt dilated convolutions to reduce the overlap region between different convolutional kernels. UNet3+ integrates high-level semantics from multi-scale feature maps with low-level semantics through full-scale skip connections. Thus, the feature map H_{de}^i of the *i*-th down-sampling layer along the direction of the encoding is computed as:

$$H_{de}^i = \begin{cases} H_{en}^i & i = N \\ \mathcal{W}\left(\begin{bmatrix} W(\mathcal{D}(H_{en}^k))_{k=i}^{i-1} \\ W(H_{en}^i) \\ W(\mathcal{U}(H_{de}^k)_{k=i+1}^N) \end{bmatrix}^T\right) & i = 1,...,N-1 \end{cases} \quad (16)$$

where H_{en}^i is the encoder feature map, $\mathcal{W}(\bullet)$ denotes the feature aggregation mechanism with convolution-BatchNorm-ReLu, $\mathcal{U}(\bullet)$ and $\mathcal{D}(\bullet)$ denote up- and down-sampling operations, respectively. We give a detailed illustration of the second decoder H_{de}^2 in Fig. 4 (b). Each decoder is composed of N scales connected, so $64 \times N$ channels are generated. Compared to UNet [34] and UNet++ [36], UNet3+ [35] has the lowest number of parameters P_{de}^i:

$$P_{de}^i = K_W \times \left[\left(\sum_{k=1}^i d(H_{en}^k) + \sum_{k=i+1}^N d(X_{de}^k)\right) \times 64 + d(H_{de}^i)^2\right] \quad (17)$$

where K_W is the kernel size of 1D-convolution and $d(\bullet)$ denotes the depth of the nodes. It is worth noting that we use dilated convolution instead of the standard convolution kernel. Dilated convolution has been validated to be effective in ECG analysis due to its ability to obtain a larger receptive field without increasing the number of covariates [37].
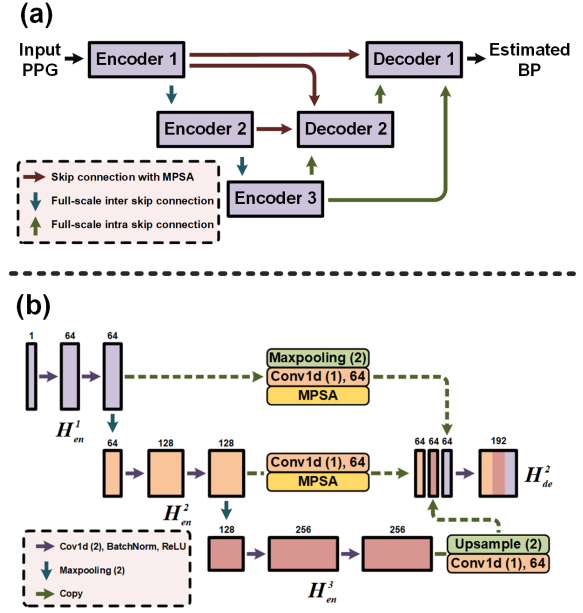

Fig. 4. Schematic diagram of the generator. (a) The UNet3+-based generator structure incorporates the MPSA attention mechanism. (b) A specific illustration of the second decoder layer H_{de}^2 for integrating full-scale aggregated feature maps.

2) PatchGAN-based Discriminator. Markov discriminators excel at maintaining ultra-high resolution and intricate details when executing style transformation [29]. Our BP waveform estimation model is inspired by this approach, where the patch-based receptive field is scaled to match the length of the PPG signals. Specifically, the discriminator convolves over the entire PPG signal, and the average response to $1 \times N$ samples is used to generate the final BP waveform output. The details of this PatchGAN-based discriminator are shown in the PPG2BP-cGAN model diagram in Fig. 1.

IV. EXPERIMENTAL SETUP

A. Data Description

We choose two datasets with paired PPG and invasive BP signals to validate the effectiveness of the proposed method, i.e., the Mindray dataset collected in our previous work [21] and the publicly available MIMIC III dataset [38]. Both are large datasets containing continuously measured vital sign parameters of ICU patients. Details of the two datasets are briefly described below:

1) Mindray Dataset [21]. The dataset was collected and screened by Mindray for usable, high-quality signals, and the invasive BP signals were obtained through intravenous needle insertion. The paired PPG and BP signals selected for this study record 683 ICU patients from 7 hospitals in 2021. The methods of measuring or recording data were strictly controlled during the collection process. PPG and invasive BP signals were sampled at 125 and 500 Hz, respectively. After filtering, outlier removal, and other preprocessing, 79,382 usable 9-second samples were obtained.

2) MIMIC (Multi-parameter Intelligent Monitoring in Intensive Care) Dataset [38]. Beth Israel Deaconess Medical

Chenbin Ma *et al*.: PPG-based Continuous BP Waveform Estimation Using Polarized Attention-guided Conditional Adversarial Learning Model

6

Center and Philips Healthcare jointly published the dataset. The MIMIC III waveform dataset contains 67,830 records from approximately 30,000 ICU patients, including ECG, BP, respiratory, and PPG waveforms. We finally selected 200 available patients with precise information data under the following sections. Here, only 20 available 30-second signals were chosen for each patient in the MIMIC dataset for 2,000 minutes of PPG-BP sample pairs.

B. Data Processing

The datasets selected for this study are all collected in an automated manner by multi-parameter monitors. These data represent a random sample of ICU patients with varying recording lengths. In particular, many signal fragments are lost in the original MIMIC dataset. Therefore, we preprocess the original dataset to screen the data for reliable quality, and Fig. 5 presents the details of the data processing process. Before the data preprocessing stage, we screen the original dataset for signals paired with PPG and invasive BP waveforms and remove fragment loss and waveform distortion data. The source of the MIMIC dataset is not recorded, so it is difficult to determine whether the signals recorded consecutively are from the same patients. In addition, the duration of signal recording varies significantly in the MIMIC dataset. To avoid model bias for too much data from the same individual, we filter only the discrete interval of 30-second signal segments labeled as the same patient. Compared to the MIMIC dataset, the data we collect from the Mindray dataset are of higher quality, with PPG-BP paired signals for each patient. Therefore, we put the entire Mindray dataset into the processing pipeline directly.

After obtaining all potentially available PPG-BP paired data, we perform signal resampling, noise reduction, phase alignment, normalization, and splitting in the preprocessing pipeline to facilitate training and inference of the deep model. In this study, we resample all signals to 100 Hz to ensure signal quality while reducing the computational burden. Next, we choose a 200-order finite impulse response filter with a cutoff

frequency of 0.5-8 Hz, which can effectively filter out power-line noise, high-frequency noise generated by muscle movement, and low-frequency noise from baseline drift. We perform phase alignment of the filtered signal to address the problem of phase delay and distortion caused by the filter. In addition, considering that the amplitude of the PPG signal can be affected by ambient light intensity, blood oxygen concentration, or venous volume, we perform maximum-minimum normalization of the PPG signal. Finally, we set a sliding window of length 512 and step size 384 to split the PPG-BP paired signals, thus ensuring a consistent length of the input model.

Validation with a small sample size dataset may produce more optimistic results [39]. Therefore, the AAMI standard has detailed requirements for the data distribution of the test set. For the intra-arterial reference, it is specified that the test set consisted of at least 150 measurements from 85 subjects and that at least 10% of SBP above 160 mmHg, 10% of SBP below 100 mmHg, 10% of DBP above 90 mmHg, and 10% of DBP below 60 mmHg [39]. We show the distribution of the processed test set after subject-wise division in Table I, which meets the AAMI standard requirements.

TABLE I
STATISTICAL DISTRIBUTION OF THE TEST SETS (SUBJECT-WISE DIVISION)

Dataset	Statistics	SBP	DBP
Mindray dataset	# of subjects/samples	290/67,474	290/67,474
	Mean ± SD (mmHg)	127.63 ± 25.80	71.25 ± 19.71
	Range (mmHg)	[50.49, 250.00]	[30.00, 149.99]
	Percentage of distribution	12.30 % < 100 mmHg 14.75 % > 160 mmHg	36.26 % < 60 mmHg 12.93 % > 90 mmHg
MIMIC dataset	# of subjects/samples	85/15,300	85/15,300
	Mean ± SD (mmHg)	124.31 ± 26.53	71.25 ± 22.69
	Range (mmHg)	[51.27, 250.00]	[32.15, 149.97]
	Percentage of distribution	13.76 % < 100 mmHg 16.33 % > 160 mmHg	28.72 % < 60 mmHg 24.58 % > 90 mmHg

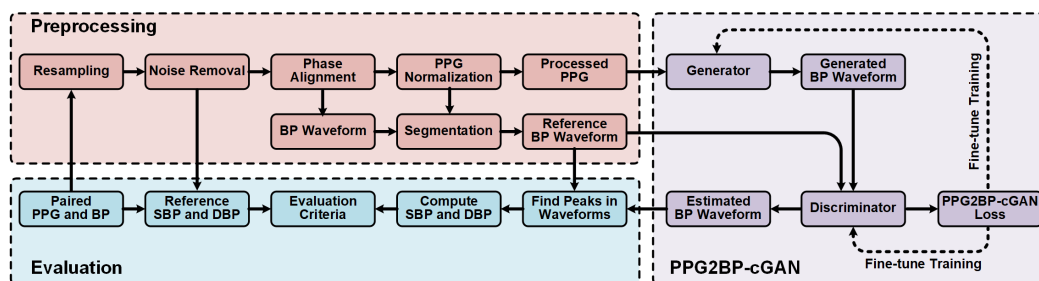**Note**, SD denote standard deviation.

Fig. 5. Flow chart of overall experimental design. The pipeline for data preprocessing of the signals includes resampling, filtering, phase alignment, normalization, and segmentation. The generator maps the input PPG signal into the BP waveform. Then the generated BP waveform and the reference BP waveform are input into the discriminator simultaneously. The estimated BP waveform continuously approximates the reference BP waveform by the adversarial learning paradigm. Finally, the corresponding SBP and DBP values are calculated and compared with clinical standards to evaluate the performance of the proposed method.

C. Training Details

This study validates the BP waveform estimation performance of the proposed model using the one-fold cross-validation method. Unlike most previous studies, we do not choose to shuffle the data samples randomly. This sample-wise paradigm could lead to the model encountering samples from the same individuals in training during testing,

making the testing error too optimistic. Therefore, this study uses an inter-subject paradigm to divide the dataset, which can ensure the reliability and generalization of the experimental results.

We used the same training setup in all experiments: the number of training rounds is 500, the learning rate of both discriminator and generator is set as 1e-3, and after every ten training epochs, the learning rate is adjusted to 0.9 times that of

Chenbin Ma *et al.*: PPG-based Continuous BP Waveform Estimation Using Polarized Attention-guided Conditional Adversarial Learning Model

7

the previous epoch. The convolution parameters were initialized by the Xavier initializer. The models were trained by using the PyTorch framework with an NVIDIA GeForce RTX 3090 GPU. The optimal hyperparameters were determined with the grid search method (e.g., the hyperparameters in the proposed jointly optimized objective function).

D. Evaluation Criteria

We use MAE and RMSE to evaluate the results of the estimated BP waveforms. These evaluation metrics are widely used in the paper and can visually represent the difference between the estimated and reference BP waveforms. The MAE and RMSE are calculated as follows:

$$MAE = \frac{1}{M} \sum_{i=1}^{M} \left(\frac{1}{L} \sum_{j=1}^{L} \left\| y_i^j - \hat{y}_i^j \right\|_1 \right) \qquad (18)$$

$$RMSE = \frac{1}{M} \sum_{i=1}^{M} \left(\sqrt{\frac{1}{L} \sum_{j=1}^{L} (y_i^j - \hat{y}_i^j)^2} \right) \qquad (19)$$

where L represents the number of sample points in the signal segment, T represents the number of segments in the test set, y represents the reference intra-arterial BP signal, and $\hat{y}$ represents the BP waveform estimated by the model for the PPG signal.

In addition, we can obtain the value of SBP/DBP within each nearly 5-second segment by calculating the average of the K peaks/valleys within the estimated BP waveform:

$$SBP = \frac{1}{K} \sum_{j=1}^{K} peak^j (\hat{y}) \qquad (20)$$

$$DBP = \frac{1}{K} \sum_{j=1}^{K} valley^j (\hat{y}) \qquad (21)$$

Here, we evaluate the performance of the estimation of BP values using the AAMI standard [39] and the BHS standard. The AAMI standard requires that the mean error (ME) is not worse than ± 5 mmHg and the SDE is not higher than 8 mmHg. The BHS standard classifies the accuracy of BP value measurement into three levels based on different prediction ranges. To achieve an A rating on the BHS, the number of samples with an estimated BP value deviating less than 5 mmHg from the reference BP value should reach 60% of the total sample size; the number of samples less than 10 mmHg should reach 85% of the total samples, and the number of samples less than 15 mmHg should reach 95% of the total samples. On the other hand, we choose commonly used classification metrics such as accuracy, specificity, sensitivity, precision, and F1 score to assess the performance of the proposed model in identifying hypertensive, normal, and hypotensive groups.

V. EXPERIMENTAL RESULTS

A. Overall Performance Evaluation

The proposed PPG2BP-cGAN requires only PPG signal input to dynamically estimate the corresponding BP waveform, so we explore its performance in BP waveform estimation, BP values prediction, and BP population classification, respectively.

1) BP Waveform Estimation. We validate the performance of the proposed method for BP waveform estimation using the Mindray dataset. Accurate BP waveform estimation can characterize detailed information about the physiology and pathology of the cardiovascular system. The RMSE of the BP waveform estimated by our proposed method on the MIMIC test set is 3.54 mmHg, the MAE is 2.86 mmHg, and the R^2 is 0.97. Fig. 6 compares the randomly selected results obtained by various models for dynamic BP waveform estimation. It can be visualized from the estimated waveforms by our proposed PPG2BP-cGAN has the highest similarity to the reference invasive BP waveform and achieves the lowest RMSE and MAE of 2.78 mmHg and 2.23 mmHg, respectively. By contrast, after replacing the generator in the cGAN model with UNet++, the RMSE and MAE increased by 164.03% and 110.31%, respectively. Similarly, deep learning models, such as V-Net based on autoencoder architecture and CycleGAN for unsupervised learning, have significant errors between the peak and trough locations of the BP waveform. In particular, for the nonlinear autoregressive models with exogenous input (NARX), there are significant errors in the prediction at the initial time, which lead to a collapse in the estimation of subsequent cycles. More comparison results between the baseline models and our proposed method are shown in our GitHub repository: https://github.com/Ma-Chenbin/SM4-PPG 2BP-cGAN.

2) BP Values Prediction. BP values are one of the most important clinical vital signs that reveal the cardiovascular health of the body by characterizing the arterial beat during the cardiac cycle. To verify that the proposed cuffless BP value estimation model meets the clinical criteria, we calculate performance regarding SBP and DBP, i.e., ME, SDE, MAE, and the percentage of estimates with MAE less than 5, 10, and 15 mmHg, respectively. As seen from the results presented in Table II, our proposed method meets the standard of AAMI and BHS. In addition, we also show the Bland-Altman plot and correlation plot in Fig. 7. The obtained results confirm the excellent performance of the model with MAE of 3.41 mmHg, 2.40 mmHg, and 2.61 mmHg for SBP, DBP, and MAP, respectively, and SDE of 4.83 mmHg, 2.77 mmHg, and 3.08 mmHg, respectively. We do not use a zero-mean calibration algorithm, but the ME values are below ± 0.73 mmHg. The results also show that more than 93.32% of the SBP, DBP, and MAP estimates have absolute errors of less than 10 mmHg compared to the reference arterial BP values.

In Fig. 7, we illustrate the high correlation between the BP values generated by the proposed model and the corresponding arterial BP values: Pearson coefficients are 0.980 and 0.941, with *p*-value < 0.001, corresponding to SBP and DBP, respectively. Correspondingly, we present the Bland-Altman plots for SBP and DBP values. These plots illustrate the mean value along with 1.96 times the standard deviation (SD), which determine the limits of agreement (LOA) between the two measurement approaches. The LOA conveys the range in which 95% of the differences between the estimations are expected to occur. Therefore, the findings demonstrate significant agreement between the estimated and reference BP values.

Chenbin Ma *et al*.: PPG-based Continuous BP Waveform Estimation Using Polarized Attention-guided Conditional Adversarial Learning Model
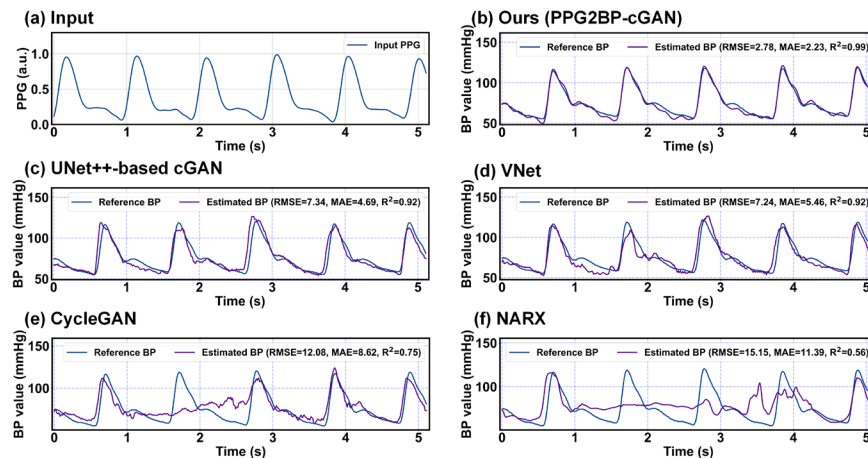
8

Fig. 6. Visualization and qualitative comparisons of different PPG-based BP waveform estimation results for the Mindray dataset with a randomly selected paired PPG signal and the corresponding reference BP waveform (The median and the worst one are shown in our GitHub repository). (a) Input normalized PPG signals and estimated BP waveforms by (b) our proposed PPG2BP-cGAN, (c) UNet++-based cGAN, (d) V-Net, (e) classical CycleGAN, and (f) NARX. For accurate validation, we evaluated the root mean square error (RMSE), mean absolute error (MAE), and Pearson coefficients (R^2) between the reference BP waveform and the estimated BP waveform.
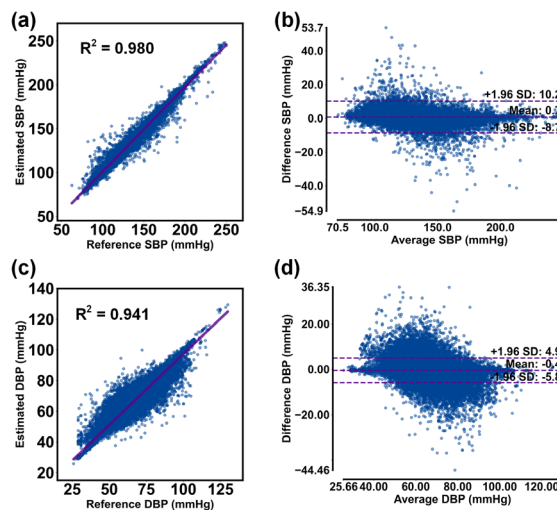

Fig. 7. The correlation and Bland-Altman plots of SBP and DBP with reference invasive BP value: (a) the correlation and (b) Bland-Altman plots in SBP estimation, (c) the correlation, and (d) Bland-Altman plots in DBP estimation.

3) Abnormal BP Identification. One of the main objectives of continuous BP monitoring is to detect abnormal changes, such as elevated or decreased BP values, as early as possible, providing a timely warning to help physicians make decisions to prevent future complications. Hypertension is a significant risk factor for cardiovascular end-organ damage, morbidity, and mortality, while hypotension is an essential indicator of inadequate tissue perfusion. Both are usually amenable to early intervention to improve the condition. Therefore, we evaluate the ability of the proposed model to identify the risk of abnormal BP in the population. We divide BP value measurements into three groups according to the American Heart Association/American College of Cardiology criteria [40] based on the experimental paradigm of Haddad et al. [41]. Specifically, we classify the BP values as hypertensive if SBP ≥ 130 mmHg and/or DBP ≥ 80 mmHg, hypotensive if SBP < 90 mmHg and/or DBP < 60 mmHg, and as normotensive otherwise. According to the BP classification criteria, the BP category for each test sample can be obtained from the SBP and DBP extracted from the estimated BP waveform. The confusion matrix of the classification results is shown in Fig. 8 (a), whose corresponding performance metrics are displayed in Table III and Table IV. The receiver operating characteristic (ROC) curves depicted in Fig. 8 (b) also demonstrate the accuracy of our model in the three specified groups. It can be found that the proposed model passes the AAMI standard in all three specific groups. Almost all groups reach grade A of the BHS, except for the hypertensive group whose SBP reaches grade B of the BHS. These results show that the model performs well in both the hypertensive and hypotensive groups, with slightly better performance in the latter. This is because hypertensive BP value worsens the PPG morphology and makes feature learning more challenging. In addition, the hypertensive group has a larger range of variation in SBP values. It obtains a lower error, which is a potential reason for failing to reach grade A of the BHS.

TABLE II
OVERALL PERFORMANCE EVALUATION OF BP VALUES ESTIMATION

	SBP	DBP	MAP
Results on Mindray Dataset			
ME (mmHg)	0.73	-0.46	-0.06
SDE (mmHg)	4.83	2.77	3.08
MAE (mmHg)	3.41	2.40	2.61
≤ 5 mmHg (%)	76.25	91.28	90.87
≤ 10 mmHg (%)	93.32	98.35	98.62
≤ 15 mmHg (%)	98.81	99.32	99.10
Results on MIMIC Dataset			
ME (mmHg)	0.72	0.41	0.51
SDE (mmHg)	4.34	2.48	2.39
MAE (mmHg)	3.15	2.21	2.12
≤ 5 mmHg (%)	80.23	92.33	91.34
≤ 10 mmHg (%)	94.58	98.76	99.20
≤ 15 mmHg (%)	99.07	99.45	99.73

TABLE III
CLASSIFICATION PERFORMANCE METRICS FOR ABNORMAL BLOOD PRESSURE IDENTIFICATION

Groups	Accuracy	Precision	Sensitivity	Specificity	F1 score
Hypertensive	99.25%	88.99%	86.76%	99.65%	87.86%
Normotensive	96.79%	96.63%	98.01%	94.99%	97.32%
Hypotensive	97.08%	97.07%	95.07%	98.28%	96.06%
Average	97.71%	94.23%	93.28%	97.64%	93.74%

Chenbin Ma *et al*.: PPG-based Continuous BP Waveform Estimation Using Polarized Attention-guided Conditional Adversarial Learning Model
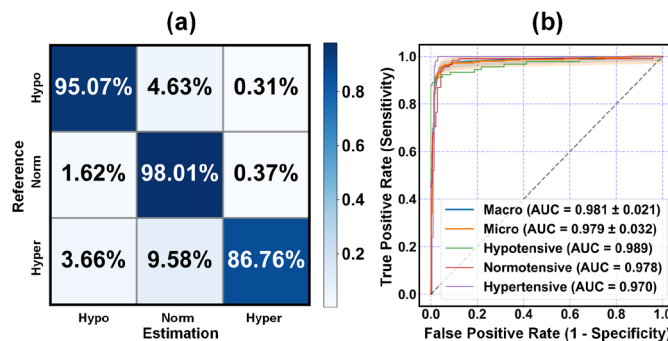
9

Fig. 8. Classification results for the abnormal BP identification. The (a) confusion matrix and (b) receiver operating characteristic (ROC) curves for the classification results. Hypo, Norm, and Hyper denote hypotensive, normotensive, and hypertensive, respectively.

TABLE IV
PERFORMANCE EVALUATION OVER DIFFERENT BLOOD PRESSURE GROUPS

	SBP			DBP		
	Hyper	Norm	Hypo	Hyper	Norm	Hypo
ME (mmHg)	1.23	-0.83	0.47	-0.93	0.45	0.33
SDE (mmHg)	7.27	5.12	3.92	4.39	2.98	2.36
MAE (mmHg)	6.33	3.61	3.55	4.04	2.54	2.15
$\leq$ 5 mmHg (%)	51.71	77.21	79.28	88.65	92.10	93.22
$\leq$ 10 mmHg (%)	76.90	94.67	94.19	96.70	98.31	98.43
$\leq$ 15 mmHg (%)	90.37	98.79	99.03	98.92	99.03	99.37

Note, Hyper, Norm, and Hypo denote hypertensive, normotensive, and hypotensive groups.

B. Robustness Performance

The above results show that our proposed PPG2BP-cGAN performs well on the Mindray dataset. By allowing clinical data to be collected across multiple hospitals, data distribution sometimes varies from center to center due to factors such as different patient characteristics, processes of care, or staff training. Therefore, models trained and tested in the Mindray dataset will have stronger generalization. To further illustrate the robustness of the proposed PPG2BP-cGAN, we explore the performance using a large single-center MIMIC dataset from different sources. In addition, we use transfer learning techniques to improve the convergence efficiency of the model to obtain better prediction performance. Specifically, we first fine-tune the deep learning model with the high-quality Mindray dataset and then transfer the pre-trained model to the target domain (i.e., the publicly available MIMIC dataset). The results of the robustness tests are shown in Table II. Our proposed PPG2BP-cGAN has the highest robustness and obtains the best prediction performance on the MIMIC dataset.

C. Ablation Study

To explore the utility of each component module in the proposed PPG2BP-cGAN model, we design some ablation experiments to quantify the effects of different hyperparameter settings on BP waveform estimation.

1) Contribution of Attention Mechanism. To assess the effectiveness of the fusion approach using spatial-temporal attention, we perform additional experiments by comparing the model without the MPSA module. In this experiment, we remove the attention module between the skip connections of the generator and keep the other network configurations unchanged during the training phase. The experimental results are shown in Table V. We can see that the ME of SBP and DBP

are reduced by 47.45% and 59.41%, respectively, and SDE is reduced by 27.18% and 40.72%, respectively, and the SDE of MAP is reduced by 36.77%, after using the MPSA attention module. Experimental results show that the attention module incorporating multi-scale features helps to mine discriminative features and improve the prediction accuracy of the model in BP values.

TABLE V
EVALUATE MODEL WITH ATTENTION MECHANISM (ME ± SDE)

Model	SBP	DBP	MAP
Without MPSA	1.37 ± 5.96	-1.01 ± 3.49	-0.22 ± 3.78
PPG2BP-cGAN	0.72 ± 4.34	0.41 ± 2.48	0.51 ± 2.39

TABLE VI
EVALUATE MODEL WITH DIFFERENT SKIP CONNECTIONS (ME ± SDE)

Model	Params	FLOPs	SBP	DBP	MAP
UNet-based	4.75	9.28	5.83 ± 12.12	-2.06 ± 5.04	0.57 ± 6.76
UNet++-based	3.06	6.78	1.65 ± 7.44	0.57 ± 4.00	0.93 ± 5.38
PPG2BP-cGAN	2.95	4.32	0.72 ± 4.34	0.41 ± 2.48	0.51 ± 2.39

Note, Params denotes the number of parameters, and the unit is mega; FLOPs denote floating-point operations, and the unit is giga.

TABLE VII
EVALUATE MODEL WITH DIFFERENT LOSS (ME ± SDE)

Hyperparameters	SBP	DBP	MAP
γ =0, $\delta = \xi$ =0	1.69 ± 6.28	0.92 ± 4.98	1.18 ± 4.21
γ =1, $\delta = \xi$ =0	1.03 ± 5.40	0.53 ± 3.87	0.70 ± 4.35
γ =0, $\delta = \xi$ =1	0.65 ± 5.05	0.39 ± 3.47	0.48 ± 4.27
γ =1, $\delta = \xi$ =1	0.72 ± 4.34	0.41 ± 2.48	0.51 ± 2.39

TABLE VIII
EVALUATE MODEL WITH DIFFERENT INPUT LENGTH (ME ± SDE)

Input Length	SBP	DBP	MAP
5 s	1.27 ± 6.96	0.82 ± 4.62	0.97 ± 4.07
7 s	1.55 ± 5.32	0.73 ± 3.43	1.00 ± 3.80
9 s	0.72 ± 4.34	0.41 ± 2.48	0.51 ± 2.39
11 s	-0.97 ± 5.15	-0.62 ± 3.14	-0.74 ± 3.12

2) Contribution of Full-scale Skip Connection. The UNet3+-based generator directly combines high-level semantics from feature maps at different scales with low-level semantics through full-scale skip connections. Table VI shows that we use the UNet and UNet++ as the backbone for the generator of cGAN to evaluate the performance. By replacing the backbone of the generator, UNet3+-based PPG2BP-cGAN uses 2.46 G, 4.96 G fewer FLOPs than the baseline cGANs while achieving several parameters below 2.11 M and 1.80 M. Therefore, we experimentally demonstrate that the proposed method has fewer parameters and faster computational efficiency than the model that uses UNet and UNet++ as generators. Similar to the findings of Huang et al. [35], we have demonstrated that the use of full-scale skip connections significantly improves BP value prediction performance over the plain skip connection-based UNet model, as indicated by the reduction in ME and SDE of SBP by 87.65% and 64.19%, respectively, compared to the reductions of ME and SDE of DBP by 80.10% and 50.79%, respectively, and MAP reduced by 64.64%. Furthermore, our proposed model surpasses UNet++ based on nested and dense skip connections. In addition, visual comparisons (shown in Fig. 6) between the estimated BP waveforms for the PPG2BP-cGAN and the UNet++-based cGAN model show that the UNet++-based cGAN model fails to capture the fine-grained features of the

Chenbin Ma *et al.*: PPG-based Continuous BP Waveform Estimation Using Polarized Attention-guided Conditional Adversarial Learning Model

10

dicrotic notch of the BP signal, leading to errors in peak and valley values and impaired estimation accuracy of critical physiological parameters such as SBP and DBP. Overall, our experimental results prove that the use of full-scale skip connections yields consistently better results compared to the single-scale skip connection structure model.

3) Contribution of Multi-loss Optimization. In our model, the hyperparameters $\lambda, \gamma, \delta, \xi \geq 0$ dominate the level of participation of a particular regularization term. These four parameters are crucial to the proposed PPG2BP-cGAN. Among them, the $\mathcal{L}_{L_1}$ loss has been shown to avoid the ambiguity problem of the generated signal [29], and we set the fixation to 1. Therefore, we conduct experiments to investigate the sensitivity of the remaining three parameters. In the first experiment, to evaluate the effect of joint multi-loss optimization, we remove all branching losses by fixing γ, δ and ξ to 0, keeping only the loss of the last fused features in the training phase. Remarkably, the hyperparameters δ and ξ reflect the degree of regularization for systolic and diastolic amplitudes, respectively, and possess similar physical significance. Additionally, the sensitivity analyses shown in our GitHub repository demonstrate that both hyperparameters exert comparable effects on BP values. Consequently, we set both to identical settings. The experimental results presented in Table VII indicate that with the inclusion of perceptual loss and the scale-specific branch loss, the ME and SDE of SBP decrease by 57.40% and 30.89%, respectively, while the ME and SDE of DBP decrease by 55.43% and 50.20%, respectively, and the ME and SDE of MAP decrease by 56.78% and 43.23%. Moreover, we added a scale-specific branch loss for SBP and DBP to evaluate the performance of classification. By taking amplitude-specific scale loss into account, the ME and SDE of SBP, DBP, and MAP decreased by 30.10%, 22.64%, and 27.14%, and by 19.63%, 35.92%, and 47.24%, respectively. These experimental outcomes illustrate that amplitude related L2 loss significantly reduces the error in BP waveform prediction. When all scale branches are optimized jointly, accuracy gradually increases. We set the coefficients of all scale branches to 1, as solely using the scale fusion branch loss (with all coefficients set to 0) is suboptimal. The recognition accuracy of deep learning features improves with increased scalar fusion branch participation, indicating that joint multi-loss optimization can improve the BP waveform estimation performance of the model.

4) Effect of Input Recording Length. According to the results presented in Table VIII, we evaluate the effect of the input recording length on the performance of PPG2BP-cGAN in estimating BP values. Specifically, we test record lengths ranging from 5 to 11 seconds. The MAE metrics of PPG2BP-cGAN for SBP, DBP, and MAP slightly decrease as the record length is increased from 5 seconds to 9 seconds.

However, as the record length is increased from 9 seconds to 11 seconds, the performance of PPG2BP-cGAN rapidly deteriorates. Consequently, we suggest that the optimal input length for PPG2BP-cGAN in estimating BP values is 9 seconds.

D. Comparison with SOTA Works

Our methodology proposes an end-to-end signal-to-signal translation method for estimating BP waveforms based on PPG. The proposed PPG2BP-cGAN makes several contributions, including a UNet3+ generator sharing full-scale parameters in PPG to extract fine and coarse physiological characteristics, dilated convolution to reduce kernel overlap, MPSA attention to extract spatial-temporal features, and joint optimization with perceptual loss and peak loss to represent low-frequency morphological features.

We compare the performance of our proposed method with SOTA works in Table IX. The experimental results show that PPG2BP-cGAN has the lowest estimation error, indicating excellent BP waveform prediction performance. Specifically, compared to NARX [14], our model has significantly lower ME and SDE regarding SBP, which are 40.00% and 52.31% higher, respectively. Our study suggests that an autoencoder model may be more suitable for signal translation tasks than a stacked convolutional module alone, as our experimental results show that the serial output of autoregressive models may collapse if a specific time step is missed.

In addition, we find that simple encoder-decoder structures, such as DCAE [18], are limited by the bottleneck structure, and the multilayer semantics in PPG is encoded as latent representation. This may result in the loss of rich semantic information in the PPG, including details of beat rhythms, peaks and valleys, and dicrotic notches associated with the BP waveform. For this reason, the UNet model incorporated with skip connection is better for predicting BP waveform. This learning paradigm has shown surprising results in image transcription, and our experiments support this conclusion. On the other hand, benefiting from a careful construction of the morphological features of the PPG signal, the Transformer-based KD-Informer [21] estimates of both SBP and DBP satisfy the AAMI standard. However, this work does not provide estimates of MAP and is not compared with the BHS standard. Additionally, cGAN models that incorporate conditional information have demonstrated superior prediction accuracy on paired datasets when compared to unsupervised CycleGAN [28]. Our experimental findings agree with this, indicating that the use of paired data is crucial for accurate PPG-based BP waveform estimation given the physiological variations among individuals, and that CycleGAN may not be capable of learning this effectively.

TABLE IX
PERFORMANCE SUMMARY OF SOTA WORKS ON BP WAVEFORM ESTIMATION (ME ± SDE)

Algorithm	# of subject	Input	Input Length	Paradigm	Calibration	SBP	DBP
WNN [22]	> 90 (MIMIC)	PPG	-	-	-	2.32 ± 2.91	1.92 ± 2.47
LSTM [23]	42 (MIMIC)	PPG	-	Sample-wise	-	-	-
NARX [14]	15 (MIMIC)	PPG, ECG	100 samples	Sample-wise	Free	-1.20 ± 9.10	-0.60 ± 4.30
DCAE [18]	18 (Custom)	PPG	5 s	Sample-wise	-	-1.66 ± 5.84	0.67 ± 3.98

Chenbin Ma *et al*.: PPG-based Continuous BP Waveform Estimation Using Polarized Attention-guided Conditional Adversarial Learning Model

11

UNet [19]	100 (MIMIC)	PPG	2.048 s	Sample-wise	Free	3.68 ± 4.42	1.97 ± 2.92
RDAE [24]	1,227 (MIMIC)	PPG	5 s	Subject-wise	Tuning	1.65 ± 6.64	-1.28 ± 3.74
UNet [25]	948 (MIMIC)	PPG	32 samples	Sample-wise	-	0.59 ± 4.78	0.43 ± 4.78
V-Net [20]	264 (MIMIC) 110 (UCLA)	PPG, ECG, handcrafted features	4 s	Subject-wise	Free Fine-tuning in MIMIC	4.30 ± 6.53 2.40 ± 5.62	-3.11 ± 4.57 -2.50 ± 3.79
CycleGAN [27]	92 (MIMIC)	PPG	2.048 s	Subject-wise	-	0.67 ± 4.52	1.78 ± 4.67
KD-Informer [21]	467 (Mindray) 241 (MIMIC)	PPG, handcrafted features	8 s	Subject-wise	Free Fine-tuning in MIMIC	0.02 ± 5.93 0.03 ± 6.38	0.01 ± 3.87 0.02 ± 4.49
PPG2BP-cGAN	683 (Mindray) 200 (MIMIC)	PPG	9 s	Subject-wise	Free Fine-tuning in Mindray	0.73 ± 4.83 0.72 ± 4.34	-0.46 ± 2.77 0.41 ± 2.48

Note, WNN denotes wavelet neural network; LSTM denotes long short-term memory; NARX denotes nonlinear autoregressive models with exogenous input; DCAE denotes deep convolutional autoencoder; RDAE denotes regularized deep autoencoder; CycleGAN denotes cycle generative adversarial network; KD-Informer denotes Transformer-based method with knowledge distillation. "-" is used where the information is not provided or the item is not used.

VI. DISCUSSION

A. Clinical Effect

Many works on PPG-based cuffless BP value prediction have emerged in recent decades. These studies hold great promise for health monitoring due to the advantages of low-cost, low-power, and non-sensitive optical signals. Most studies fit the BP values by machine learning models using manual extraction of morphological features from PPG and/or ECG [4-8, 12-17]. These efforts rely heavily on signal processing, feature design, and feature selection associated with expert experience. They compress the high-dimensional physiological signal into an abstract single-valued feature vector, which may ignore the coupling details of the nonlinearity in vascular dynamics. The predictive performance of these studies gradually reaches a bottleneck considering the inadequate learning capability of shallow models. In addition, obtaining BP values such as SBP and DBP alone is not sufficient to describe the fluctuation of BP in humans.

With the development of deep learning, some works have started to explore the mapping connection between PPG and BP signals, and these advanced works are shown in Table IX. These models can directly output estimated BP waveforms by inputting PPG and/or ECG signal sequences, thus obtaining continuous dynamic BP waveforms. BP waveforms contain a wealth of physiological and pathological information about the human cardiovascular system. For example, the BP waveform can reflect factors such as the pumping function of the heart, the resistance and elasticity of the peripheral vessels, the systemic blood volume, and the physical state of the blood [32]. Therefore, accurate measurement of BP waveforms has an essential clinical role in disease prevention and diagnosis. However, the available studies still have some deficiencies, and our proposed method has better clinical utility, specifically:

1) Only PPG signal is needed. Fewer inputs mean that only simple sensors are required and will significantly reduce computational complexity. Some studies that require ECG signals require additional impedance electrodes to be attached, increasing the burden on the user [14, 20].

2) No handcrafted features. Although the V-Net [20] and KD-Informer [21] can estimate BP waveforms accurately, it requires additional extraction of statistical features of the input signal. This increases the difficulty of data collection in clinical scenarios and brings additional computational costs.

3) Subject-wise-based data division paradigm. The paradigm of randomly shuffled samples may lead to more optimistic results when trained models are tested with data from the same individuals [14, 18, 19]. Therefore, in medical data modeling, ensuring that training and test sets contain data from different subjects can avoid the risk of data leakage.

4) Validation on multiple large datasets. Validation on large and differently sourced datasets is necessary to avoid overfitting problems in the model and assess the robustness of the estimated BP waveform performance. A total of 883 patients are used, and the results of the tests on different datasets prove the validity and reliability of our proposed model. According to the AAMI standard, the validation set based on invasive BP waveforms as the reference should contain data from a minimum of 15 subjects, while the appropriate sample size is 85 subjects. However, some studies do not meet this requirement [14, 18].

5) No calibration is required. Most studies have found calibration algorithms to result in lower BP waveform prediction errors [11, 13-16, 42, 43]. The BP waveform estimation model proposed by Hill et al. [20] requires additional calibration of the cuff-based oscillometric method, which may be inconvenient. In addition, some of the studies do not disclose whether calibration values are used [18, 27]. Our model achieves better estimation results without calibration and dramatically improves clinical usability.

B. Model Applicability

Recent works on BP waveform estimation using deep learning models have shown improved accuracy in estimation. Various network models have demonstrated different performance levels. Comparison results in Table IX indicate that the prediction performance of NARX, based on an autoregressive model, is significantly lower than that of models with autoencoder architecture. This may be because signal translation tasks require fine-grained waveform details, and the autoregressive model, limited by the time step of the input, struggles to capture long-term memorized information. Furthermore, visualized waveform plots in Fig. 6 show that a prediction error at a single time step can lead to subsequent prediction crashes. In contrast, encoder-decoder architecture models learn a compressed representation of the input PPG signal to identify global features, and then reconstruct the signal from the latent representation while modifying the waveform's local features. Therefore, encoder-decoder architecture improves this problem. However, autoencoders used to compress PPG signals may lose some minor physiological variability characteristics, especially when dealing with PPG signals with large variations in frequency and amplitude range. This is because autoencoders tend to focus on

Chenbin Ma *et al*.: PPG-based Continuous BP Waveform Estimation Using Polarized Attention-guided Conditional Adversarial Learning Model

12

reducing reconstruction error rather than preserving subtle signal features. Hence, it is crucial to design the compression process carefully to avoid losing important physiological information during data compression.

Based on these principles, our proposed PPG2BP-cGAN introduces adversarial learning to enhance the estimation process. Specifically, we construct a UNet3+-based generator to continuously learn the probability distribution of the input PPG signals in the training set, so the distribution of the estimated BP waveform approximates the distribution of the real invasive BP waveform as closely as possible. The discriminator, based on PatchGAN, observes both reference and estimated BP waveforms to discriminate the truth from the input data. Through alternate training iterative confrontation, both the generator and discriminator are enhanced until equilibrium is reached, and the trained generator can generate high-quality BP waveforms. Experimental results demonstrate that our proposed method outperforms SOTA works.

C. Limitations

This study has identified several limitations that require attention in future research. Firstly, limiting datasets to those obtained solely from ICU patients raises concerns about the generalizability of our findings to other populations, such as healthy individuals or those taking antihypertensive medication. Secondly, the validity of our work depends heavily on the preprocessing of PPG signals, whose acquisition can be influenced by environmental factors in complex usage scenarios. Thirdly, using invasive BP waveforms as the supervised signal for training the model may lead to inconsistencies between the BP values measured by cuff-based devices. Moreover, because of incomplete data, the proposed model did not incorporate demographic information for all participants. Finally, the amount of data required to train our model is substantially larger than that needed for classical machine learning models. These limitations should be considered when interpreting and applying our model's results in practice. Future research should aim to address these limitations, improve the robustness and efficiency of the model, and explore ways to incorporate cuffless BP measurements into the training process.

VII. CONCLUSION

Our study introduces a novel attention-guided cGAN-based end-to-end deep learning approach for estimating cuffless BP waveforms from PPG signals. The PPG2BP-cGAN model utilizes adversarial learning to ensure that the predicted BP waveform is similar to the reference BP waveform. Our work introduces conditional variables to mitigate the collapse problem that may arise during the training process of the model, which is one of the major contributions of our study. The ablation studies show that the attentional mechanism significantly enhances the performance of the UNet3+-based generator. In particular, the MPSA module, which is based on the spatial-temporal attention mechanism, improves the generator's capability to capture both spatial and temporal features of the input PPG signal. We designed a discriminator comprising PatchGAN to enhance the discriminative ability of

the generated signal by enlarging the perceptual field of the generated BP signal using full convolution structures.

Our experimental results demonstrate that our proposed method outperforms the state-of-the-art methods on two distinct datasets, indicating the high reliability and robustness of our methodology for BP waveform estimation. By performing continuous cuffless monitoring of the BP waveform of each cardiac cycle and tracking the trend of BP changes over time, our proposed method can provide valuable physiological information that can aid in the effective prevention and diagnostic treatment of cardiovascular ailments.

REFERENCES

[1] K. ReFaey *et al.*, "Cancer Mortality Rates Increasing vs Cardiovascular Disease Mortality Decreasing in the World: Future Implications," *Mayo Clinic Proceedings: Innovations, Quality & Outcomes,* vol. 5, no. 3, pp. 645-653, 2021/06/01/ 2021, doi: 10.1016/j.mayocpiqo.2021.05.005.

[2] A. Timmis *et al.*, "European Society of Cardiology: cardiovascular disease statistics 2021," *European Heart Journal,* vol. 43, no. 8, pp. 716-799, 2022, doi: 10.1093/eurheartj/ehab892.

[3] S. L. Stevens *et al.*, "Blood pressure variability and cardiovascular disease: systematic review and meta-analysis," *BMJ,* vol. 354, p. i4098, 2016, doi: 10.1136/bmj.i4098.

[4] S. S. Mousavi, M. Firouzmand, M. Charmi, M. Hemmati, M. Moghadam, and Y. Ghorbani, "Blood pressure estimation from appropriate and inappropriate PPG signals using A whole-based method," *Biomedical Signal Processing and Control,* vol. 47, pp. 196-206, 2019/01/01/ 2019, doi: 10.1016/j.bspc.2018.08.022.

[5] M. Panwar, A. Gautam, D. Biswas, and A. Acharyya, "PP-Net: A Deep Learning Framework for PPG-Based Blood Pressure and Heart Rate Estimation," *IEEE Sensors Journal,* vol. 20, no. 17, pp. 10000-10011, 2020, doi: 10.1109/JSEN.2020.2990864.

[6] C. El-Hajj and P. A. Kyriacou, "Deep learning models for cuffless blood pressure monitoring from PPG signals using attention mechanism," *Biomedical Signal Processing and Control,* vol. 65, p. 102301, 2021/03/01/ 2021, doi: 10.1016/j.bspc.2020.102301.

[7] G. Slapničar, N. Mlakar, and M. Luštrek, "Blood Pressure Estimation from Photoplethysmogram Using a Spectro-Temporal Deep Neural Network," *Sensors,* vol. 19, no. 15, p. 3420, 2019, doi: 10.3390/s19153420.

[8] N. Aguirre, E. Grall-Maës, L. J. Cymberknop, and R. L. Armentano, "Blood Pressure Morphology Assessment from Photoplethysmogram and Demographic Information Using Deep Learning with Attention Mechanism," *Sensors,* vol. 21, no. 6, p. 2167, 2021, doi: 10.3390/s21062167.

[9] J. E. Johnson, O. Shay, C. Kim, and C. Liao, "Wearable Millimeter-Wave Device for Contactless Measurement of Arterial Pulses," *IEEE Transactions on Biomedical Circuits and Systems,* vol. 13, no. 6, pp. 1525-1534, 2019, doi: 10.1109/TBCAS.2019.2948581.

[10] J. Joseph, P. Nabeel, M. I. Shah, and M. Sivaprakasam, "Arterial compliance probe for calibration free pulse pressure measurement," in *2016 IEEE International Symposium on Medical Measurements and Applications (MeMeA)*, Benevento, Italy, 15-18 May 2016 2016: IEEE, pp. 1-6, doi: 10.1109/MeMeA.2016.7533810.

[11] H. Eom *et al.*, "End-To-End Deep Learning Architecture for Continuous Blood Pressure Estimation Using Attention Mechanism," *Sensors,* vol. 20, no. 8, p. 2338, 2020, doi: 10.3390/s20082338.

[12] S. Shimazaki, S. Bhuiyan, H. Kawanaka, and K. Oguri, "Features Extraction for Cuffless Blood Pressure Estimation by Autoencoder from Photoplethysmography," in *2018 40th Annual International Conference of the IEEE Engineering in Medicine and Biology Society (EMBC)*, 18-21 July 2018 2018, pp. 2857-2860, doi: 10.1109/EMBC.2018.8512829.

[13] S. Baek, J. Jang, and S. Yoon, "End-to-End Blood Pressure Prediction via Fully Convolutional Networks," *IEEE Access,* vol. 7, pp. 185458-185468, 2019, doi: 10.1109/ACCESS.2019.2960844.

[14] C. Landry, S. D. Peterson, and A. Arami, "Nonlinear Dynamic Modeling of Blood Pressure Waveform: Towards an Accurate Cuffless Monitoring System," *IEEE Sensors Journal,* vol. 20, no. 10, pp. 5368-5378, 2020, doi: 10.1109/JSEN.2020.2967759.

[15] M. S. Tanveer and M. K. Hasan, "Cuffless blood pressure estimation from electrocardiogram and photoplethysmogram using waveform based

This article has been accepted for publication in IEEE Journal of Biomedical and Health Informatics. This is the author's version which has not been fully edited and content may change prior to final publication. Citation information: DOI 10.1109/JBHI.2023.3324319

Chenbin Ma *et al*.: PPG-based Continuous BP Waveform Estimation Using Polarized Attention-guided Conditional Adversarial Learning Model

13

ANN-LSTM network," *Biomedical Signal Processing and Control,* vol. 51, pp. 382-392, 2019/05/01/ 2019, doi: 10.1016/j.bspc.2019.02.028.

[16] C. Yan *et al.*, "Novel Deep Convolutional Neural Network for Cuff-less Blood Pressure Measurement Using ECG and PPG Signals," in *2019 41st Annual International Conference of the IEEE Engineering in Medicine and Biology Society (EMBC)*, 23-27 July 2019 2019, pp. 1917-1920, doi: 10.1109/EMBC.2019.8857108.

[17] S. Shimazaki, H. Kawanaka, H. Ishikawa, K. Inoue, and K. Oguri, "Cuffless Blood Pressure Estimation from only the Waveform of Photoplethysmography using CNN," in *2019 41st Annual International Conference of the IEEE Engineering in Medicine and Biology Society (EMBC)*, 23-27 July 2019 2019, pp. 5042-5045, doi: 10.1109/EMBC.2019.8856706.

[18] M. Sadrawi *et al.*, "Genetic Deep Convolutional Autoencoder Applied for Generative Continuous Arterial Blood Pressure via Photoplethysmography," *Sensors,* vol. 20, no. 14, p. 3829, 2020, doi: 10.3390/s20143829.

[19] T. Athaya and S. Choi, "An Estimation Method of Continuous Non-Invasive Arterial Blood Pressure Waveform Using Photoplethysmography: A U-Net Architecture-Based Approach," *Sensors,* vol. 21, no. 5, p. 1867, 2021, doi: 10.3390/s21051867.

[20] B. L. Hill *et al.*, "Imputation of the continuous arterial line blood pressure waveform from non-invasive measurements using deep learning," *Scientific Reports,* vol. 11, no. 1, p. 15755, 2021/08/03 2021, doi: 10.1038/s41598-021-94913-y.

[21] C. Ma *et al.*, "KD-Informer: Cuff-Less Continuous Blood Pressure Waveform Estimation Approach Based on Single Photoplethysmography," *IEEE Journal of Biomedical and Health Informatics,* vol. 27, no. 5, pp. 2219-2230, 14 June 2022 2022, doi: 10.1109/JBHI.2022.3181328.

[22] P. Li *et al.*, "Novel wavelet neural network algorithm for continuous and noninvasive dynamic estimation of blood pressure from photoplethysmography," *Science China Information Sciences,* vol. 59, no. 4, p. 042405, 2015/09/25 2015, doi: 10.1007/s11432-015-5400-0.

[23] C. Sideris, H. Kalantarian, E. Nemati, and M. Sarrafzadeh, "Building Continuous Arterial Blood Pressure Prediction Models Using Recurrent Networks," in *2016 IEEE International Conference on Smart Computing (SMARTCOMP)*, 18-20 May 2016 2016, pp. 1-5, doi: 10.1109/SMARTCOMP.2016.7501681.

[24] K. Qin, W. Huang, and T. Zhang, "Deep generative model with domain adversarial training for predicting arterial blood pressure waveform from photoplethysmogram signal," *Biomedical Signal Processing and Control,* vol. 70, p. 102972, 2021/09/01/ 2021, doi: 10.1016/j.bspc.2021.102972.

[25] K. R. Vardhan, S. Vedanth, G. Poojah, K. Abhishek, M. N. Kumar, and V. Vijayaraghavan, "BP-Net: Efficient Deep Learning for Continuous Arterial Blood Pressure Estimation using Photoplethysmogram," in *2021 20th IEEE International Conference on Machine Learning and Applications (ICMLA)*, 13-16 Dec. 2021 2021, pp. 1495-1500, doi: 10.1109/ICMLA52953.2021.00241.

[26] R. Mukkamala *et al.*, "Toward Ubiquitous Blood Pressure Monitoring via Pulse Transit Time: Theory and Practice," (in eng), *IEEE transactions on bio-medical engineering,* vol. 62, no. 8, pp. 1879-901, Aug 2015, doi: 10.1109/tbme.2015.2441951.

[27] M. A. Mehrabadi, S. A. H. Aqajari, A. H. A. Zargari, N. Dutt, and A. M. Rahmani, "Novel Blood Pressure Waveform Reconstruction from Photoplethysmography using Cycle Generative Adversarial Networks," presented at the 2022 44th Annual International Conference of the IEEE Engineering in Medicine & Biology Society (EMBC), Glasgow, Scotland, United Kingdom, 11-15 July 2022, 2022.

[28] J.-Y. Zhu, T. Park, P. Isola, and A. A. Efros, "Unpaired image-to-image translation using cycle-consistent adversarial networks," in *Proceedings of the IEEE international conference on computer vision*, 2017 2017, pp. 2223-2232.

[29] P. Isola, J.-Y. Zhu, T. Zhou, and A. A. Efros, "Image-to-image translation with conditional adversarial networks," in *Proceedings of the IEEE conference on computer vision and pattern recognition*, 2017, pp. 1125-1134.

[30] X. Ding, Y. Zhang, J. Liu, W. Dai, and H. K. Tsang, "Continuous Cuffless Blood Pressure Estimation Using Pulse Transit Time and Photoplethysmogram Intensity Ratio," *IEEE Transactions on Biomedical Engineering,* vol. 63, no. 5, pp. 964-972, 2016, doi: 10.1109/TBME.2015.2480679.

[31] W. Chen, T. Kobayashi, S. Ichikawa, Y. Takeuchi, and T. Togawa, "Continuous estimation of systolic blood pressure using the pulse arrival time and intermittent calibration," *Medical Biological Engineering Computing,* vol. 38, no. 5, pp. 569-574, 2000.

[32] M. F. O'Rourke, "Arterial pressure waveforms in hypertension," (in eng), *Minerva Med,* vol. 94, no. 4, pp. 229-250, 2003/08// 2003.

[33] H. Liu, F. Liu, X. Fan, and D. Huang, "Polarized self-attention: Towards high-quality pixel-wise mapping," *Neurocomputing,* vol. 506, pp. 158-167, 28 September 2022 2022, doi: 10.1016/j.neucom.2022.07.054.

[34] O. Ronneberger, P. Fischer, and T. Brox, "U-net: Convolutional networks for biomedical image segmentation," in *Medical Image Computing and Computer-Assisted Intervention–MICCAI 2015: 18th International Conference, Munich, Germany, October 5-9, 2015, Proceedings, Part III 18*, 2015: Springer, pp. 234-241.

[35] H. Huang *et al.*, "Unet 3+: A full-scale connected unet for medical image segmentation," in *ICASSP 2020-2020 IEEE International Conference on Acoustics, Speech and Signal Processing (ICASSP)*, Barcelona, Spain, 04-08 May 2020 2020: IEEE, pp. 1055-1059, doi: 10.1109/ICASSP40776.2020.9053405.

[36] Z. Zhou, M. M. Rahman Siddiquee, N. Tajbakhsh, and J. Liang, "Unet++: A nested u-net architecture for medical image segmentation," in *Deep Learning in Medical Image Analysis and Multimodal Learning for Clinical Decision Support: 4th International Workshop, DLMIA 2018, and 8th International Workshop, ML-CDS 2018, Held in Conjunction with MICCAI 2018, Granada, Spain, September 20, 2018, Proceedings 4*, 20 September 2018 2018, vol. 11045: Springer, pp. 3-11, doi: 10.1007/978-3-030-00889-5_1.

[37] M. S. Islam, K. F. Hasan, S. Sultana, S. Uddin, J. M. Quinn, and M. A. Moni, "HARDC: A novel ECG-based heartbeat classification method to detect arrhythmia using hierarchical attention based dual structured RNN with dilated CNN," *Neural Networks,* vol. 162, pp. 271-287, May, 2023 2023, doi: 10.1016/j.neunet.2023.03.004.

[38] A. E. W. Johnson *et al.*, "MIMIC-III, a freely accessible critical care database," *Scientific Data,* vol. 3, no. 1, p. 160035, 2016/05/24 2016, doi: 10.1038/sdata.2016.35.

[39] A. f. t. A. o. M. Instrumentation, "American national standards for electronic or automated sphygmomanometers," *ANSI/AAMI SP,* pp. 10-1987, 1987.

[40] R. D. Toto, "Defining Hypertension: Role of New Trials and Guidelines," (in eng), *Clin J Am Soc Nephrol,* vol. 13, no. 10, pp. 1578-1580, 2018, doi: 10.2215/CJN.05350418.

[41] S. Haddad, A. Boukhayma, and A. Caizzone, "Continuous PPG-Based Blood Pressure Monitoring Using Multi-Linear Regression," *IEEE Journal of Biomedical and Health Informatics,* vol. 26, no. 5, pp. 2096-2105, 2022, doi: 10.1109/JBHI.2021.3128229.

[42] B. Huang, W. Chen, C.-L. Lin, C.-F. Juang, and J. Wang, "MLP-BP: A novel framework for cuffless blood pressure measurement with PPG and ECG signals based on MLP-Mixer neural networks," *Biomedical Signal Processing Control,* vol. 73, p. 103404, 2022, doi: 10.1016/j.bspc.2021.103404.

[43] Y.-H. Li, L. N. Harfiya, K. Purwandari, and Y.-D. Lin, "Real-Time Cuffless Continuous Blood Pressure Estimation Using Deep Learning Model," *Sensors,* vol. 20, no. 19, 2020, doi: 10.3390/s20195606.